FORMATION OF PRIMORDIAL GALAXIES UNDER ULTRAVIOLET BACKGROUND RADIATION

HAJIME SUSA[1] AND MASAYUKI UMEMURA[2]
Center for Computational Physics, University of Tsukuba, Tsukuba 305, Japan

ABSTRACT

The pancake collapse of pregalactic clouds under UV background radiation is explored with a one-dimensional sheet model. Here, attention is concentrated on elucidating the basic physics on the thermal evolution of pregalactic clouds exposed to diffuse UV radiation. So, we treat accurately the radiation transfer for the ionizing photons, with solving chemical reactions regarding hydrogen molecules as well as atoms. The self-shielding against UV radiation by H_2 Lyman-Werner bands, which regulates the photodissociation of hydrogen molecules, is also taken into account. As a result, it is found that when the UV background radiation is at a level of $10^{-22}(\nu/\nu_L)^{-1}$ ergs s^{-1} cm^{-2} Hz^{-1} sr^{-1}, the cloud evolution bifurcates with a critical mass as $M_{SB} = 2.2 \times 10^{11} M_\odot [(1 + z_c)/5]^{-4.2}$, where z_c is the final collapse epoch. A cloud more massive than M_{SB} cools below 5×10^3 K owing to H_2 line emission at the pancake collapse and would undergo the initial starburst. The pancake possibly evolves into a virialized system in a dissipationless fashion. Consequently, this leads to the dissipationless galaxy formation at $3 \lesssim z_c \lesssim 10$. A cloud less massive than M_{SB} cannot cool by H_2 emission shortly after the pancake collapse but could cool in the course of shrinking to the rotation barrier. This is likely to lead to the dissipational galaxy formation at relatively low redshifts as $0 \lesssim z_c \lesssim 4$. The present results provide a solid physical mechanism that controls the star formation efficiency in the pregalactic clouds. In the context of a standard CDM cosmology, M_{SB} lies between 1σ and 2σ density fluctuations.

Subject headings: galaxies: formation — molecular processes — radiative transfer — shock heating

1. INTRODUCTION

It has been widely accepted that the formation of the first generation of objects, say Population III objects, is regulated by the cooling of primordial hydrogen molecules. A number of authors have explored the formation of Population III objects in so-called dark age ($z > 5$) by concentrating on the role of hydrogen molecules (Matsuda, Sato, & Takeda 1965; Yoneyama 1972; Hutchins 1976; Carlberg 1981; Palla, Salpeter, & Stahler 1983; Susa, Uehara, & Nishi 1996; Uehara et al. 1996; Annonis & Norman 1996; Tegmark et al. 1997; Nakamura & Umemura 1999). Also, even if the gas contains metals, the metallic line cooling is overwhelmed by the hydrogen/helium cooling at $T > 10^4$ K when the metallicity is lower than $10^{-2} Z_\odot$ (Böhringer & Hensler 1989). In fact, recently, the metal abundance in intergalactic space is inferred to be at a level of $10^{-3} Z_\odot$ (Cowie et al. 1997; Songaila & Cowie 1996; Songaila 1997; Cowie & Songaila 1998). Moreover, at lower temperatures of $T < 10^4$ K, the H_2 cooling is estimated to be still predominant as long as the metallicity is lower than $10^{-2} Z_\odot$, from the comparison of the cooling of the solar abundance gas (Spitzer 1978, p. 143) with the maximal H_2 cooling (Kang & Shapiro 1992). Hence, hydrogen molecules are likely to play a fundamental role on the formation of galaxies in the metal-poor environment.

In addition, there seem to be situations in which UV background radiation significantly influences the dynamical as well as thermal evolution of pregalactic clouds. At the epochs of $z < 5$, the existence of UV background of $10^{-21 \pm 0.5}$ ergs s^{-1} cm^{-2} sr^{-1} Hz^{-1} at the Lyman limit is inferred from the so-called proximity effect of the Lyα forest (Bajtlik, Duncan, & Ostriker 1988; Giallongo et al. 1996). Also, the Gunn-Peterson optical depths show that the intergalactic space was, in fact, highly ionized (Gunn & Peterson 1965; Schneider, Schmidt, & Gunn 1989, 1991). The UV background is attributed to the radiation from quasars and partially from young galaxies (e.g., Giallongo et al. 1996). Even in the dark age of the universe, say $z > 5$, the first generation of objects as well as unseen protoquasars might be external photoionization sources for subsequently collapsing objects. So far, many authors have considered the dynamical effects produced by the UV background radiation (Umemura & Ikeuchi 1984; Dekel & Rees 1987; Babul & Rees 1992; Efstathiou 1992; Chiba & Nath 1994; Thoul & Weinberg 1996; Quinn, Katz, & Efstathiou 1996; Navarro & Steinmetz 1997) to account for Lyα clouds or to reconcile the paradox that in the hierarchical clustering paradigm for galaxy formation, low-mass galaxies are over-produced compared with observations (White & Frenk 1991; Kauffman, White, & Guiderdoni 1993; Cole et al. 1994). The simulations have been hitherto based upon the assumption that the medium is optically thin against UV photons. However, the gas clouds become optically thick as the gravitational collapse proceeds. The significance of the optical depth has been stressed by the accurate treatment on radiative transfer (Tajiri & Umemura 1998).

The primary effects of UV radiation are photoionization, UV heating, and photodissociation of H_2 (Haiman, Rees, & Loeb 1996, hereafter HRL; Haiman, Rees, & Loeb 1997; Corbelli, Galli, & Palla 1997; Kepner, Babul, & Spergel 1997). HRL, with including radiation transfer effects in one-zone clouds, estimated the UV heating rate and the cooling rate under the assumption of the chemical equilibrium. They found that the cooling rate can exceed the heating rate at $T \lesssim 10^4$ K for high density. However, basically the chemical reactions regarding H_2 formation are not in equilibrium (e.g., Susa et al. 1998; Bertoldi & Draine 1996;

[1] susa@rccp.tsukuba.ac.jp.
[2] umemura@rccp.tsukuba.ac.jp.

Diaz-Miller, Franco, & Shore 1998; Hollenbach & Tielens 1999). In particular, if ionization processes such as shock heating or photoionization take place, the chemical processes become out of equilibrium (e.g., Shapiro & Kang 1987). Thus, the nonequilibrium process for the formation of H_2 should be involved, coupled with hydrodynamical process.

In this paper, we reexamine the thermal and dynamical evolution of pregalactic clouds under UV background radiation. In the present analysis, we solve properly the radiative transfer of diffuse UV photons and include nonequilibrium chemical reactions regarding H_2 formation owing to shock ionization and photoionization. The goal is to elucidate the key physics on the effects of the UV background radiation upon the thermal evolution of pregalactic clouds. For the purpose, we make the dynamical model as simple as possible. A cosmological density perturbation far beyond the Jeans scale forms a flat pancake-like disk. Although the pancake formation is originally studied by Zeldovich (1970) in the context of the adiabatic fluctuations in baryon or hot dark matter–dominated universes, recent numerical simulations have shown that such pancake structures also emerge in a CDM cosmology (e.g., Cen et al. 1994). Thus, the pancakes are thought to be a ubiquitous feature in gravitational instability scenarios. Here, we consider pancakes in the plane-parallel symmetry. Also, previous one-, two-, and three-dimensional simulations on the pancake collapse in a dark matter–dominated universe show that the pancake is finally dominated by baryons after the caustics (Shapiro, Struck-Marcell, & Melott 1983; Bond et al. 1984; Shapiro & Struck-Marcell 1985; Yuan, Centrella, & Norman 1991; Umemura 1993; Cen et al. 1994; Miralda-Escude & Rees 1994; Hernquist et al. 1995; Zhang, Anninos, & Norman 1995; Anninos & Norman 1996). The presence of dark matter increases the shock velocity of the falling matter into the caustics. According to previous analyses (e.g., Shapiro & Kang 1987), such shocks change the thermal evolution in the absence of a UV background when the temperature exceeds 10^4 K since the temperature controls H_2 fraction in the postshock regions. However, under UV background radiation, the difference of shock velocity will not alter the results significantly because the sheets are initially ionized by UV radiation and therefore quickly heated up to $\sim 10^4$ K. Thus, the thermal evolution of the shocked region will be rather similar for any infall velocity, regardless of the shock temperature. Thus, in order to highlight the relevant physics of thermal processes, we deliberately exclude the dark matter contribution. Nonetheless, some dynamical effects are anticipated from dark matter, e.g., Jeans instability. They are discussed later in the light of the present results.

In § 2, we describe the basic equations and initial conditions. In § 3, the numerical results are presented. In § 4, we make the physical interpretation of numerical results and present the condition on the cooling of a collapsing pancake. Section 5 is devoted to the implications for galaxy formation under UV background radiation. In the last section, we summarize the results.

2. FORMULATION

2.1. *Basic Equations*

In this section, we give the basic equations for hydrodynamical calculations. We assume the plane-parallel sym-

metry throughout this paper. A set of the ordinary hydrodynamical equations is given below:

$$\frac{d(1/\rho)}{dt} - \frac{\partial u}{\partial m} = 0 \, , \tag{1}$$

$$\frac{du}{dt} + \frac{\partial p}{\partial m} = g \, , \tag{2}$$

$$\frac{dE}{dt} + \frac{\partial(up)}{\partial m} = ug - \Lambda(\rho, T, y_i) \, , \tag{3}$$

where ρ, p, u, and z denote the density, the thermal pressure, the velocity, and the length measured from the midplane, respectively, and E is the total energy per unit mass,

$$E = \frac{p}{\rho(\gamma - 1)} + \frac{u^2}{2} \, , \tag{4}$$

$m(z)$ is the column density,

$$m(z) \equiv \int_0^z \rho(z)dz \, , \tag{5}$$

and g is the gravitational acceleration,

$$g \equiv 2\pi Gm(z) \, . \tag{6}$$

The symbol $\Lambda(\rho, T, y_i)$ denotes the cooling rate minus heating rate per unit mass owing to the radiative and chemical processes of the ith species. We take the H_2 cooling rate from Hollenbach & Mckee (1979), and the other atomic cooling Z rates are the same as those in Shapiro & Kang (1987), except the cooling rate concerning helium. Photoheating rate is calculated by taking into account the radiation transfer effects. The formulation is given in the Appendix. The equation of state is assumed as $p = \rho kT/\mu_M$, where k denotes the Boltzmann constant, and μ_M is the mean molecular weight of the five species discussed below in this section. The hydrodynamical equations are solved by the piecewise parabolic method (PPM) described in Colella & Woodward (1984). PPM is one of the accurate methods to resolve the strong shock front. We take typically 800 spatial Lagrange grids. The hydrodynamical routine is tested by the Sod's problem. This code resolves the shock front typically by a few mesh.

In equations (1), (2), and (3), the cosmic expansion is neglected. It is because we have considered the massive clouds far beyond the Jeans scale $\{\lambda_J \sim 10[(1 + z)/10]^{-1.5}$ kpc$\}$ and also postulated that the initial stage is close to the maximum expansion for a density fluctuation. The effects of the cosmic expansion could be important for a density perturbation near the Jeans scale, since the temperature is raised up to $\sim 10^4$ K by UV background radiation in spite of the expansion, and consequently the dynamics could be significantly influenced by the UV heating (e.g., Umemura & Ikeuchi 1984). However, far beyond the Jeans scale, the thermal pressure of gas around 10^4 K anyway does not affect the dynamical evolution until the maximum expansion as shown by previous calculations (e.g., Thoul & Weinberg 1996). Therefore, we attempt to pursue the history after the maximum expansion.

The hydrodynamical equations are coupled with the nonequilibrium rate equations for chemical reactions:

$$\frac{dy_i}{dt} = \sum_j k_j y_j + n \sum_{k,l} k_{kl} y_k y_l + n^2 \sum_{m,n,s} k_{mns} y_m y_n y_s \, , \tag{7}$$

where y_i is the fraction of i-th species, $y_i \equiv n_i/n$, with n being the number density of hydrogen nuclei, and k's are the coefficients of reaction rates (see Table 1). In the present calculations, we take into account six species: e, H, H^+, H^-, H_2, and H_2^+. Here, we neglect helium. This is because the helium lines are not an effective coolant for lower temperature ($T \lesssim 10^4$ K) in which we are especially interested here. Nonetheless, some of helium lines including recombination lines may affect the ionization structure because they are energetic enough to ionize H I. However, according to Osterbrock (1989, 17–29), the difference between the ionization structure of pure hydrogen and hydrogen + helium gas for 40,000 K blackbody radiation is small. In the case of the power-law spectrum of UV background radiation that we consider, the difference could be larger because the higher energy photons contribute more to the ionization of helium compared to the case of blackbody radiation. In fact, in the recent calculation by Abel & Haehnelt (1999), in which the radiation transfer effects of helium recombination photons are taken into account, the temperature of the clouds could differ by a factor of 2. Although we have dismissed helium to focus upon elucidating the key physics, we should keep in mind that helium could be important in highly quantitative arguments.

The photoionization and heating processes due to the external UV radiation are pursued by solving the frequency-dependent radiative transfer equation for hydrogen,

$$\mu \frac{dI_\nu}{dz} = -\kappa_\nu I_\nu + \eta_\nu \,, \qquad (8)$$

TABLE 1

REACTION RATES

Reactions	References
$H^+ + e \rightarrow H + \gamma$	1
$H + e \rightarrow H^- + \gamma$	2
$H^- + H \rightarrow H_2 + e$	3
$3H \rightarrow H_2 + H$	4
$H_2 + H \rightarrow 3H$	5
$2H + H_2 \rightarrow 2H_2$	4
$2H_2 \rightarrow 2H + H_2$	5
$H + e \rightarrow H^+ + 2e$	6
$2H \rightarrow H + H^+ + e$	5
$H + H^+ \rightarrow H_2^+ + \gamma$	7
$H_2^+ + H \rightarrow H_2 + H^+$	8
$H_2 + H^+ \rightarrow H_2^+ + H$	9
$H^- + H^+ \rightarrow H_2^+ + e$	10
$H_2^+ + e \rightarrow 2 H$	11
$H_2^+ + H^- \rightarrow H + H_2$	9
$H^- + e \rightarrow H + 2e$	12
$H^- + H \rightarrow 2H + e$	13
$H^- + H^+ \rightarrow 2H$	12
$H + \gamma \rightarrow H^+ + e$	14
$H_2 + \gamma \rightarrow 2H$	15

REFERENCES.—(1) Spitzer 1956, p. 88; (2) de Jong 1972; (3) Beiniek 1980; (4) Palla, Salpeter, & Stahler 1983; (5) SK; (6) Lotz 1968; (7) Ramaker & Peek 1976; (8) Karpas, Anicich, & Huntress 1979; (9) Prasad & Huntress 1980; (10) Poularert et al. 1978; (11) Mitchell & Deveau 1983; (12) Duley & Williams 1984; (13) Izotov & Kolensnik 1984; (14) See text; (15) Draine & Bertoldi 1996.

where μ, κ_ν, and η_ν denote the direction cosine, the absorption coefficient, and the emissivity, respectively. The frequency-integration in the transfer equation can be done analytically for the continuum, while the recombination line near the Lyman limit is separately treated by solving transfer equation with a source term which comes from the recombination. The details are described in the Appendix. Equation (8) assumes steadiness of the radiation fields. When a neutral cloud is exposed to background ionizing radiation, ionized regions spread inward. In the ionized regions, the radiation propagates basically at the light speed, which is typically 10^3 times larger than the hydrodynamical velocity of the system. Thus, as for the radiation fields, it is sufficient to solve the steady radiative transfer equation. However, the ionization front propagates with a different speed, which is determined by the balance between the number of neutral atoms flowing through the front per second and the corresponding number of ionizing photons reaching the front. As a result, the speed of ionization front is much lower than the light speed, typically 500 km s^{-1} $(n/10^{-2}$ cm$^{-3})^{-1}$ for UV background of 10^{-21} ergs s^{-1} cm^{-2} sr^{-1} Hz^{-1}. In order to capture the ionization front propagation, we take the following numerical procedures. First, the steady radiative transfer equation (8) is solved, in which typically 800 spatial grids are used, a number that is equivalent to the number of Lagrange meshes assigned for hydrodynamics, and 40 angular grids are adopted. We have checked that the resultant accuracy is not significantly changed if we use the larger number of angular grids. The integration of equation (8) is performed with the summation of the exact formal solution in every grid (Stone, Miharas, & Norman 1992). This method is accurate, even if the optical depth of each grid can exceed unity. Also, the validity of this method is enhanced by the fact that the ionization front is not sharply edged but, rather, fairly dull for a power law of UV radiation (Tajiri & Umemura 1998). For the photons that cause H_2 dissociation through the Solomon process (e.g., HRL), we employ the self-shielding function given by Draine & Bertoldi (1996), instead of directly solving the radiation transfer equation. Next, the rate equations including photoionization are solved implicitly for a time step, which is determined as below. Finally, the hydrodynamical equations including the thermal equation are integrated explicitly.

The time step of the calculation Δt is taken as follows:

$$\Delta t = \min (0.99 t^{\mathrm{hydro}}, 0.8 t^{\mathrm{grav}}, 0.3 t^{\mathrm{cool}}, 0.3 t^{\mathrm{heat}}) \,. \qquad (9)$$

Here, t^{hydro} represents the hydrodynamical time, and $0.99 t^{\mathrm{hydro}}$ is employed so that the Courant condition is satisfied. t^{grav} denotes the timescale of gravity, which is defined as $t^{\mathrm{grav}} \equiv (p/\gamma\rho)^{1/2}/|g|$, where p, γ, ρ, and g represent the pressure, the adiabatic index, the density, and the gravitational acceleration, respectively. t^{cool} and t^{heat} represent the local cooling time and heating timescale, respectively. With these procedures, we have checked the propagation speed of the ionization front defined by the point $y_{\mathrm{H\,I}} = 0.1$. In all of our simulations, the I-front propagation speeds are less than 1% of the speed of light. Thus, the assumption of the steady radiation transfer is valid.

2.2. Initial Conditions

We assume the initial density distributions to have a

cosine profile:

$$n_{\rm ini}(z) = \bar{n}_{\rm ini}[1 + \varepsilon \cos (\pi z/\lambda)] \, , \tag{10}$$

where $\bar{n}_{\rm ini}$ and λ are the initial mean number density and the thickness of the sheet (see Fig. 1), and ε denotes the density contrast, which is set to be 0.5 throughout this paper. The ranges of $\bar{n}_{\rm ini}$ and λ that we consider are 10^{-6} cm$^{-3} \leq \bar{n}_{\rm ini} \leq 5 \times 10^{-2}$ cm^{-3} and 0.3 kpc $\leq \lambda \leq 3$ Mpc, respectively. The initial velocity is null for every mass layer because the initial stage is implicitly assumed to be close to the maximum expansion stage of a density fluctuation. In general, an overdense region at the maximum expansion is surrounded by an underdense region that is still expanding. Hence, if we introduce the initial velocity distributions more realistically, additional mass may accrete from the underdense region after the pancake collapse. However, the envelope does not seem to contribute to the self-shielding because of its low density, and thus the self-shielding is determined by the column density of the first collapsed sheet. Hence, we neglect the surrounding expanding underdense region and model only the overdense region. Moreover, the velocity gradient may exist in a collapsing overdense region, and then this leads to the delay of mass accretion from outer regions. The degree of self-shielding is determined by the total recombination number per unit time ($N_{\rm rec}$) in the volume against the UV photon number per unit time ($N_{\rm UV}$) from the boundary. If the envelope has a density distribution in proportion to r^x, $N_{\rm rec}$ is proportional to r^{2x+1}, whereas $N_{\rm UV}$ is constant, as far as the envelope undergoes nearly sheetlike collapse. Thus, an envelope with a distribution steeper than $r^{-1/2}$ would not contribute to the self-shielding. In other words, the inner regions that collapse nearly simultaneously contribute mainly to the self-shielding. Although there are such qualitative expectations, we cannot assess accurately the effects by the initial velocity gradient and the cosmological expansion because we have not included them. They should be quantitatively investigated in the future analyses.

The initial temperature and chemical composition are given respectively by the thermal equilibrium and by the ionization equilibrium. Also, the fractions of H_2, H^-, and H_2^+ are initially determined by the chemical equilibrium. When determining the initial equilibrium state, the H_2

FIG. 1.—Profile for the initial density distributions. The horizontal axis, z, is the height from the midplane. The vertical axis is the number density, $n_{\rm ini}$. $\bar{n}_{\rm ini}$ and λ denote the mean number density of the slab and the wavelength of the slab, respectively. ε is the parameter that characterizes the initial density contrast (see the text).

cooling rate is ignored because we set the initial condition so that the UV heating should overwhelm the H_2 cooling. It will be shown below that this condition can be satisfied even if the cloud is almost neutral.

The incident radiation intensity, $I_\nu^{\rm in}$, is assumed to have a power-law spectrum as

$$I_\nu^{\rm in} = I_{21}(\nu/\nu_{\rm L})^{-\alpha}10^{-21} \text{ ergs s}^{-1} \text{ cm}^{-2} \text{ sr}^{-1} \text{ Hz}^{-1} \, , \tag{11}$$

where $\nu_{\rm L}$ is the frequency at the Lyman limit. The observations require the diffuse UV radiation to be at a level of $I_{21} = 10^{\pm 0.5}$ at $z = 1.7$–4.1 (Bajtlik, Duncan, & Ostriker 1988; Giallongo et al. 1996). At higher redshifts, we have no indication for I_{21}. Here, we assume $I_{21} = 0.1$, and the scaling to $I_\nu^{\rm in}$ is argued. As for α, two typical cases are considered, i.e., $\alpha = 1$ or 5, which are the same choices as made by Thoul & Weinberg (1996). The former represents a quasar-like spectrum, and the latter resembles a spectrum of star-forming galaxies around the Lyman limit frequency.

3. THERMAL AND DYNAMICAL EVOLUTION

In this section, we show the characteristic behaviors of the thermal/dynamical evolution resulting from numerical runs and elucidate the dependence of the final states upon the initial states.

3.1. *Hard Spectrum Case: $\alpha = 1$*

Figures 2 and 3 show the time evolution of spatial distributions of various physical quantities in the case of $\alpha = 1$. Figure 2 represents the case with $\lambda = 100$ kpc and $\bar{n}_{\rm ini} = 10^{-2}$ cm^{-3}. In this figure, each horizontal axis represents the Lagrange coordinate, normalized by the half-total surface density, m_0. The thick line shows the distribution at $t = 1.28/(4\pi G\bar{\rho}_{\rm ini})^{1/2}$, where $\bar{\rho}_{\rm ini} = m_p \bar{n}_{\rm ini}$, with m_p being the proton mass. The calculations are terminated there. Figure 2 shows that, in the course of the collapse, a thin cold sheet quickly forms as a result of the efficient molecular cooling, which is confined by a shock-heated high-temperature layer. The lower panels in Figure 2 show the corresponding H I and H_2 distributions. Only an outer envelope ($m/m_0 \gtrsim 0.9$) is photoionized and the remaining parts of the sheet are self-shielded against UV radiation. As a result, the sheet is mostly neutral throughout the dynamical evolution, excepting the collisionally ionized postshock regions. In the early phase, UV heating exceeds the H_2 line cooling even in the almost neutral regions. The H_2 cooling becomes efficient as the collapse proceeds to a further degree, and finally the temperature drops down to ~ 100 K. Then, the collisional dissociation of hydrogen molecules becomes ineffective, and thus the fraction of hydrogen molecules at $m = 0$ continues to increase.

Figure 3 represents the case with lower density and larger size, i.e., $\bar{n}_{\rm ini} = 5 \times 10^{-5}$ cm^{-3} and $\lambda = 1$ Mpc. The sheet also collapses because the initial thickness is larger than the initial Jeans length. However, the central temperature does not drop below $\sim 10^4$ K, and the resultant H_2 fraction is too low to overwhelm the UV heating. Why the evolution results in different final states from the case shown in Figure 2 is basically understood by the difference of the degree of self-shielding against the external UV radiation. In the previous case, most regions are so strongly shielded from the external UV that abundant H_2 forms and the cooling rate resulting from H_2 becomes predominant. Contrastively, in the present case, the external UV permeates the inner regions to a considerable degree, so that UV heating over-
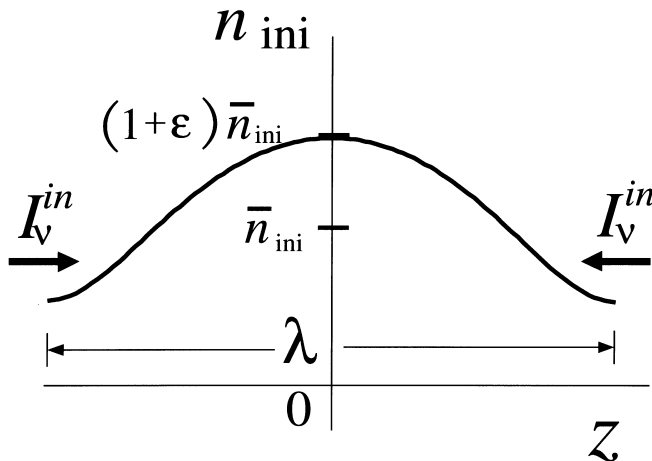
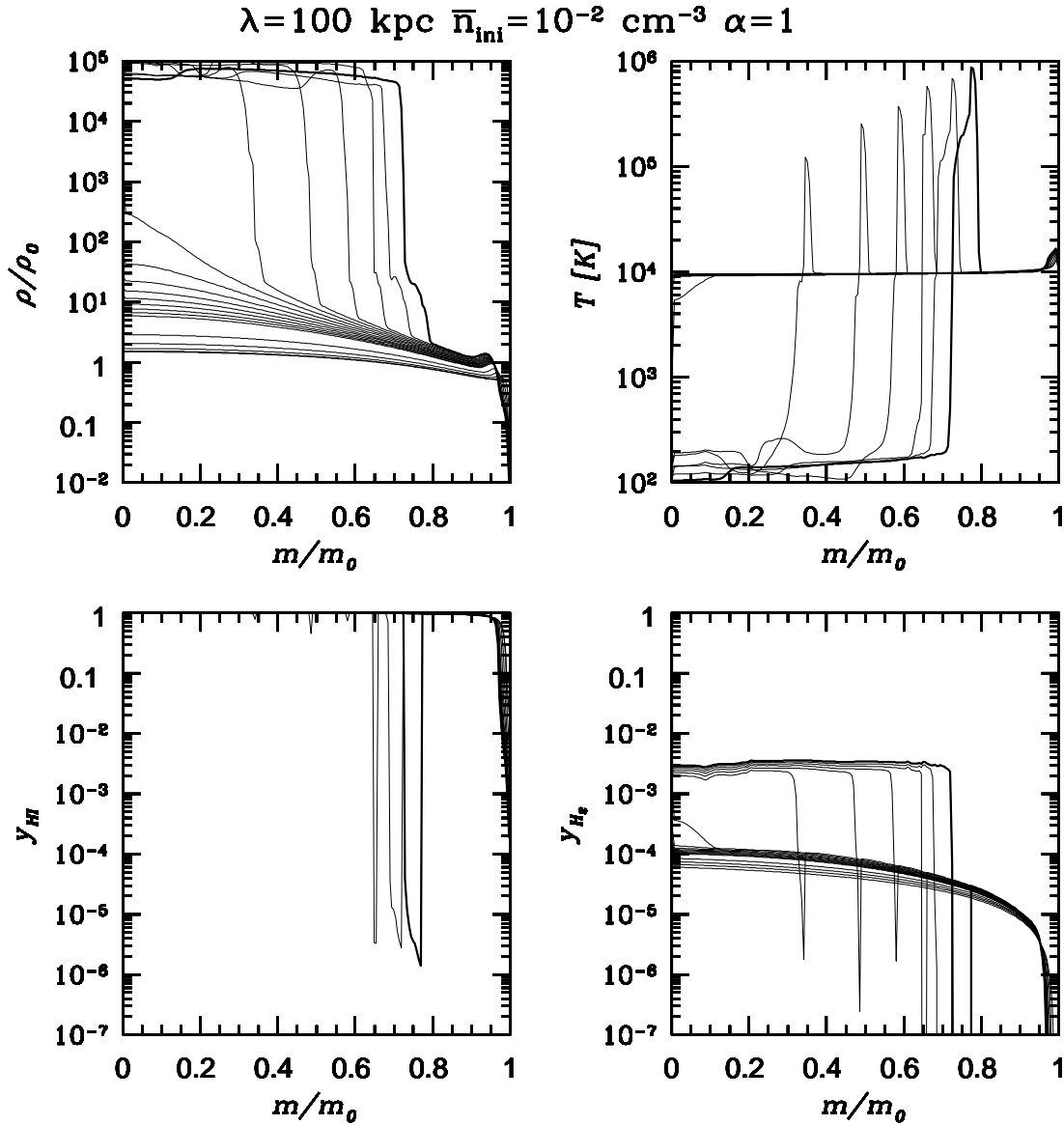## $\lambda=100$ kpc $\bar{n}_{\mathrm{ini}}=10^{-2}$ cm^{-3} $\alpha=1$

Fig. 2.—Time evolution of the spatial distributions for various physical quantities is presented in the case of $\bar{n}_{\mathrm{ini}} = 10^{-2}$ cm^{-3}, $\lambda = 100$ kpc, and $\alpha = 1$. The horizontal axis in each panel is the Lagrange coordinate normalized by the half-total surface density, m_0. Note that $m/m_0 = 0$ corresponds to the midplane of the sheet and $m/m_0 = 1$ is the surface. The upper left-hand panel shows the density distributions and the upper right-hand panel shows the temperature distributions. The lower left-hand panel is the distributions for H I fraction, and the lower right-hand panel shows the distributions for H$_2$ fraction. The thick solid lines show the final stage, i.e., $t = 1.28 \times (4\pi G\bar{\rho}_{\mathrm{ini}})^{-1/2}$, where $\bar{\rho}_{\mathrm{ini}} = m_p \bar{n}_{\mathrm{ini}}$.

whelms H$_2$ cooling everywhere until the collapse stops owing to the thermal pressure.

3.2. Soft-Spectrum Case: $\alpha = 5$

Figure 4 shows the case of a softer spectrum, $\alpha = 5$. The other initial parameters are the same as those in Figure 3. Compared to the previous hard-spectrum cases, the inner parts of the sheet are quickly self-shielded as the collapse proceeds. This is due to the fact that there are fewer high-energy photons that penetrate deeply inside the sheet owing to the smaller ionization cross section (see, e.g., Tajiri & Umemura 1998). As a result, the photoionization rate as well as the UV heating rate damps strongly in the inner regions, so that a cold layer ($T < 10^4$ K) owing to H$_2$ cooling emerges eventually. The self-shielded regions grow thicker, and the fraction of H$_2$ goes up to a level of 10^{-3} similar to the case of Figure 2.

3.3. Summary of the Dependence on Initial States

In Figure 5, the final physical states of the sheets for $\alpha = 1$ at $t = 1.28/(4\pi G\bar{\rho}_{\mathrm{ini}})^{1/2}$ are summarized on the initial density-to-size diagram. Depending upon the initial thickness λ and mean density $\bar{n}_{\mathrm{ini}}$, the sheets evolve in different ways. Filled circles in Figure 5 denote the initial conditions on which the clouds eventually cool below 5×10^3 K during the collapse. Open circles denote the ones on which the clouds cannot cool ($T > 5 \times 10^3$ K). The boundary of the evolutionary bifurcation is well fitted by a simple power-law relation as

$$\lambda_{\mathrm{cool}} = 1.1 \text{ Mpc}\left(\frac{\bar{n}_{\mathrm{ini}}}{1.0 \times 10^{-4} \text{ cm}^{-3}}\right)^{-0.8}. \quad (12)$$

The small open squares, open triangles, and filled triangles in Figure 5 trace the evolutionary paths for three typical
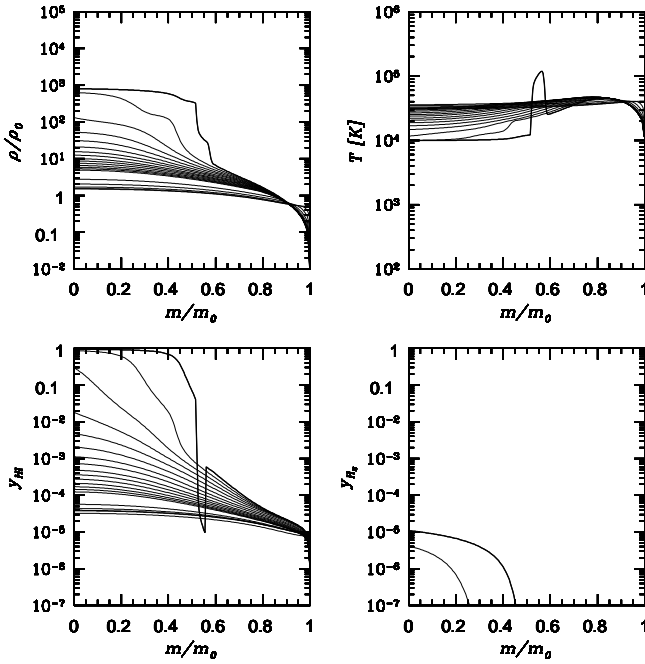
FIG. 3.—Same as Fig. 2, except that $\bar{n}_{\rm ini} = 5 \times 10^{-5}$ cm^{-3}, $\lambda = 1$ Mpc.

parameters. In the paths, the time-dependent thickness (H) is defined by the thickness within which 80% of the total mass of the sheet is contained, and the time-dependent mean density ($\bar{n}$) is defined by the spatially averaged density over H:

$$H \equiv 2 \int_0^{0.9 m_0} \frac{1}{\rho} \, dm \, , \qquad (13)$$

$$\bar{n} \equiv \frac{2}{H} \int_0^H n \, dz \, . \qquad (14)$$

The open squares and open triangles are the results for the initial parameters of $(\lambda, \bar{n}_{\rm ini}) = (1$ Mpc, 5×10^{-5} cm$^{-3})$ and $(100$ kpc, 1×10^{-3} cm$^{-3})$, respectively. For such initial conditions, the sheet shrinks due to Jeans instability $[\lambda > \lambda_J(T = 10^4$ K$)]$. However, the collapse ceases by the thermal pressure before it intersects the critical line marked by $\lambda_{\rm shield}$, above which the sheet can be self-shielded and cool down owing to formed H$_2$. (Further details on $\lambda_{\rm shield}$ are discussed in the next section.) On the other hand, the filled triangles, corresponding to the run with $(\lambda, \bar{n}_{\rm ini}) = (100$ kpc, 1×10^{-2}cm$^{-3})$, come into the regions $\lambda > \lambda_{\rm shield}$ before the thermal pressure prevents the sheet from collapsing. Consequently, this sheet is shielded and cools below $T \sim 5 \times 10^3$ K.

Figure 6 shows the dependence on the initial states for $\alpha = 5$. Because of the smaller number of runs, it is somewhat hard to divide clearly the parameter space. If we dare to draw the boundary, it is proportional to $\bar{n}_{\rm ini}^{-0.66}$, which is numerically

$$\lambda_{\rm cool} = 6.0 \times 10^2 \ {\rm kpc} \left(\frac{\bar{n}_{\rm ini}}{1.0 \times 10^{-4} \ {\rm cm}^{-3}} \right)^{-0.66} . \qquad (15)$$

This criterion is slightly different from the previous case, in the sense that $\lambda_{\rm cool}$ for $\alpha = 5$ does not cross the intersection point of $\lambda_J(T = 10^4$ K$) = \lambda_{\rm shield}$, although $\lambda_{\rm cool}$ for $\alpha = 1$ does.

4. PHYSICAL CONDITIONS FOR H$_2$ COOLING UNDER UV BACKGROUND

In this section, we attempt to understand the underlying physics of the present numerical results. To begin with, we introduce a scale, $\lambda_{\rm shield}$, which characterizes the relative efficiency of the H$_2$ cooling to the UV heating. Then, coupled with some physical arguments, we try to estimate the boundary of the bifurcation, $\lambda_{\rm cool}$, which has been derived by the present numerical calculations.

As a measure of the penetration of UV photons into the cloud, a shielding length, $\lambda_{\rm shield}$, is defined by the balance between the UV heating rate and the H$_2$ cooling rate, which are, respectively,

$$\text{Heating rate} = n(z) y_{\rm H\,I} \Gamma_{\rm H\,I}[\tau_{\nu_L, \nu}(z)] \, , \qquad (16)$$

$$\text{Cooling rate} = n(z)^2 \Lambda_{\rm H_2}[y_{\rm H_2}(z), \, T(z)] \, , \qquad (17)$$

where $\Gamma_{\rm H\,I}$ is the UV heating rate per particle, and $\Lambda_{\rm H_2}$ denotes the H$_2$ cooling function. As shown in the Appendix (eq. [A12]), in an optically thick regime, the UV heating rate is expressed by a power law of the optical depth at the Lyman limit, not by an exponential law. This is again because higher energy photons have the smaller ionization cross section. The optical depth at the Lyman limit measured from the outer boundary ($z = z_{\rm out}$) is

$$\tau_{\nu_L, \nu}(z) \equiv \int_z^{z_{\rm out}} dz \, n y_{\rm H\,I} \sigma_{\nu_L} \, , \qquad (18)$$

where σ_ν is the ionization cross section. If the slab is almost neutral,

$$\tau_{\nu_L, \nu}(0) \simeq \int_0^{z_{\rm out}} dz n \sigma_{\nu_L} \, , \qquad (19)$$

$$= \bar{n}_{\rm ini} \sigma_{\nu_L} \lambda/2 \, . \qquad (20)$$

Equating (16) with equation (17) at the midplane of the slab ($z = 0$) and also using equations (20) and (A12), we can assess $\lambda_{\rm shield}$ as

$$\lambda_{\rm shield} \simeq \frac{2}{\bar{n}_{\rm ini} \sigma_{\nu_L}} \left[\frac{2\pi I_{\nu_L}^{\rm in} \sigma_{\nu_L} \nu_L}{3 \bar{n}_{\rm ini} \Lambda_{\rm H_2}} \frac{\Gamma(\beta)}{1 + \beta} \right]^{1/\beta} \propto \bar{n}_{\rm ini}^{-1 - 1/\beta} \, , \qquad (21)$$

where $\beta \equiv 1 + (\alpha - 1)/3$. The $\lambda_{\rm shield}$ is plotted in Figures 5 and 6 by long-dashed lines. The cooling rate has been assumed to be $\Lambda_{\rm H_2} = 10^{-26}$ cm^3 s^{-1}, which is a maximal value of H$_2$ cooling for the primordial gas that is once heated up to $T \gtrsim 10^4$ K (Shapiro & Kang 1987; Susa et al. 1998).

The obtained $\lambda_{\rm shield}$ represents the degree of self-shielding against the external UV at the initial stages: (1) For $\lambda > \lambda_{\rm shield}(\bar{n}_{\rm ini})$, the sheet is promptly self-shielded enough to be cooled by the H$_2$. (2) For $\lambda < \lambda_{\rm shield}(\bar{n}_{\rm ini})$, the sheet is not self-shielded initially, so that the gas is heated up to $T \gtrsim 10^4$ K owing to predominant UV heating. A similar argument with $\lambda_{\rm shield}$ is also applicable to each dynamical stage. In this case, we should just replace the density $\bar{n}_{\rm ini}$ by $\bar{n}$ and λ by H, both of which are defined in § 3. Then, we interpret $\lambda_{\rm shield}$ as the boundary beyond which the sheet is quickly self-shielded and consequently cools down owing to the efficient formation of H$_2$. In fact, the clouds denoted by filled circles in Figure 5 satisfy the condition $H > \lambda_{\rm shield}$ before the collapse is abruptly decelerated by approaching $\lambda_J(T = 10^4$ K$)$. Eventually, the clouds cool down below 5×10^3 K. On the other hand, the clouds denoted by open circles

$$\lambda = 10^3 \text{ kpc } \bar{n}_{ini} = 5 \times 10^{-5} \text{ cm}^{-3} \alpha = 5$$
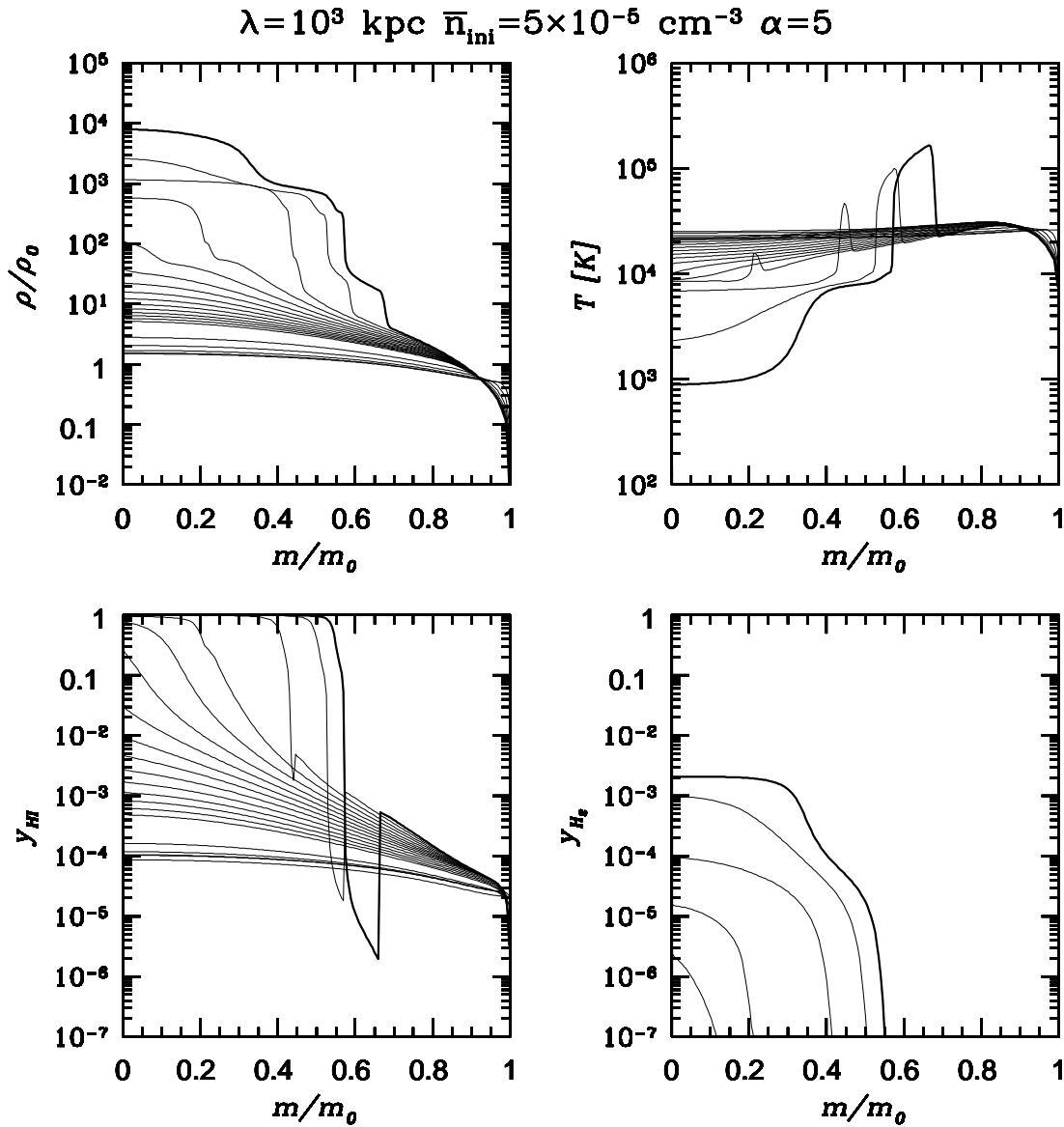
FIG. 4.—Same as Fig. 2, except that $\alpha = 5$

above λ_J in Figure 5 result in warm sheets of $\sim 10^4$ K, because the clouds first meet $\lambda_J (T = 10^4$ K) before intersect λ_{shield}. If we assume that the sheet clouds evolve keeping the relation $\bar{n}H = $ const as anticipated in the ideal sheet collapse, the boundary of the bifurcation in the space $(\bar{n}_{ini}, \lambda)$ is expected to be a line which satisfies $\bar{n}_{ini} \lambda = $ const and meets the intersection point of $\lambda_{shield} = \lambda_J$. This prediction, $\lambda_{cool} \propto \bar{n}_{ini}^{-1}$, is close to the numerically obtained boundary, $\lambda_{cool} \propto \bar{n}_{ini}^{-0.8}$. The small difference of the dependence may come from the fact that the simulations contain the spatial structure of density and temperature and therefore partial self-shielding.

We remark that the Jeans length λ_J is maximally scaled by $(\Omega_B/\Omega_0)^{1/2}$ in the presence of dark matter, where Ω_B is the baryon density parameter, and Ω_0 is the total density parameter. However, the baryonic component dominates the gravity of the sheets in the final phase of the collapse, although dark matter component does initially. Thus, what actually happens is the intermediate of these two extreme cases. Although calculations that include dark matter are

necessary to evaluate the effect quantitatively, we leave them to be done elsewhere.

5. IMPLICATIONS FOR GALAXY FORMATION

Based upon the present numerical results, we consider the context of the galaxy formation under UV background radiation. First of all, the cooling by atomic processes of primordial gas is essential for the formation of H_2 molecules that control the star formation in primordial objects. The elaborate analyses by Rees & Ostriker (1977) and also by Blumenthal et al. (1984) show that the cooling mass is roughly constant almost regardless of the virial temperature and density, which is $\sim 10^{12} M_\odot$. If there is UV background radiation, the cooling mass could alter because the line cooling by H and He at $\lesssim 10^5$ K is seriously reduced (e.g., Thoul & Weinberg 1996). The mass, however, is basically determined by the cooling mechanisms at $\gtrsim 10^5$ K. At such a temperature, the cooling in photoionized gas is dominated by collisional ionization, radiative recombination, and thermal bremsstrahlung, and possibly the
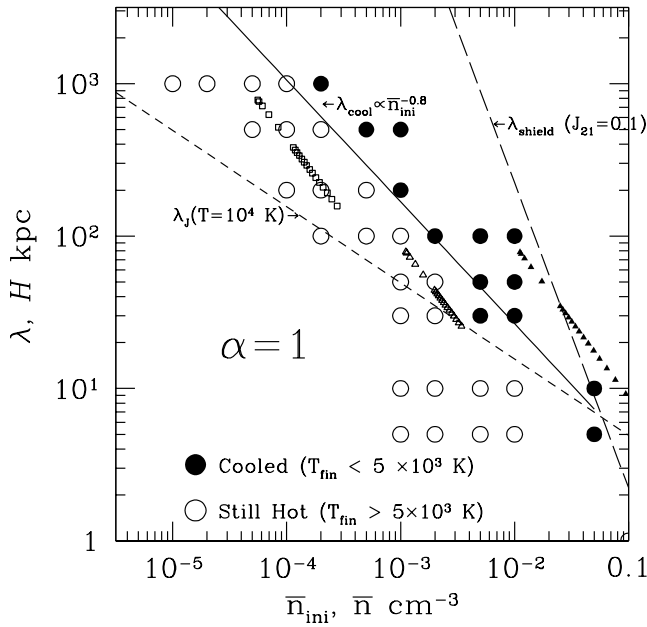
FIG. 5.—Physical states at $t = 1.28/(4\pi G\rho_{ini})^{1/2}$ with given initial parameters are summarized. The vertical axis and the horizontal axis denote the thickness and the mean density of the sheets. The open and filled circles represent the initial conditions for the runs which we performed. The open circles denote the sheets whose central temperature is high ($T > 5 \times 10^3$ K) after one dynamical time. The sheets denoted by the filled circles have cooled below 5×10^3 K. Solid line (λ_{cool}) denotes the boundary of the cold sheets and the hot ones. Long-dashed line (λ_{shield}) denotes the critical thickness above which the sheets are initially self-shielded against external UV heating. Short-dashed line is the Jeans length with $T = 10^4$ K. Small open squares, open triangles, and filled triangles represent the evolutionary sequences for three initial parameters (see text).

Compton cooling at high redshifts. These mechanisms may potentially cool the clouds with $\sim 10^{12}$ $M_\odot$ down to several 10^4 K. In fact, it is shown by numerical calculations that the clouds with $\sim 10^{12}$ $M_\odot$ can cool and collapse under UV background (Umemura & Ikeuchi 1984). Thus, we set here the upper mass of primordial galaxies to be 10^{12} $M_\odot$. Then,
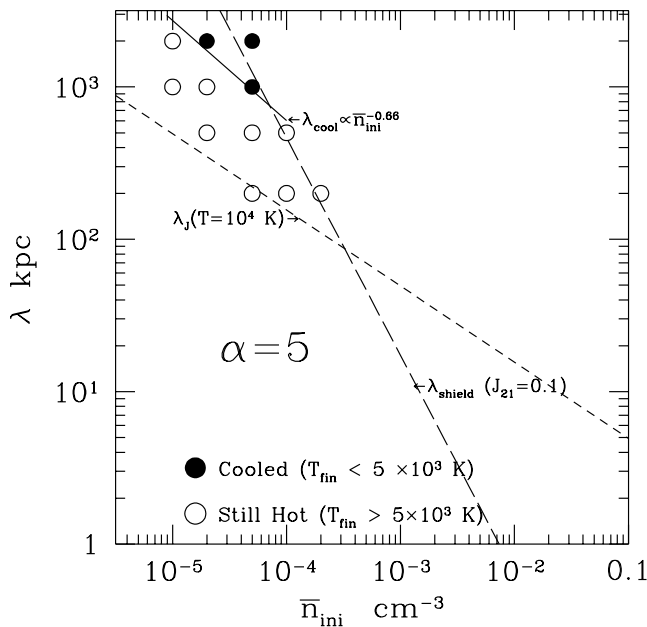

FIG. 6.—Same as Fig. 5, except $\alpha = 5$

the evolution of pregalactic clouds under UV background radiation is discriminated into four categories: (a) promptly self-shielded clouds, (b) starburst pancakes, (c) retarded star-forming galaxies, and (d) expanding clouds. In Figure 7, the parameter regions corresponding to the four categories are shown for $\alpha = 1$, with lines of equal mass, say, 10^8 $M_\odot$ and 10^{12} $M_\odot$. The upper abscissa is the collapse redshifts, z_c, if the initial stage is assumed to be at the maximum expansion of a spherical top-hat density fluctuation. $\Omega_0 = 1$, $h = 0.5$, and $\Omega_B h^2 = 0.02$ are assumed in order to interpret the maximal expansion density into the collapse redshift z_c, where h is the present Hubble constant in units of 100 km s^{-1} Mpc^{-1}. In this figure, 1 σ, 2 σ, and 3 σ density fluctuations expected in a standard CDM are also shown. Some further details for each category are discussed in the following, restricting ourselves to the case $\alpha = 1$.

5.1. Promptly Shielded Clouds

The evolution of promptly self-shielded clouds above λ_{shield} is virtually equivalent to the evolution under no UV background radiation. The collapse redshifts of such clouds are expected to be $z_c \gtrsim 10$. The formation of primordial objects under no UV background has been hitherto extensively studied by numerous authors (Matsuda, Sato, & Takeda 1965; Yoneyama 1972; Hutchins 1976; Palla, Salpeter, & Stahler 1983; Susa, Uehara, & Nishi 1996; Anninos & Norman 1996; Tegmark et al. 1997). As a result,
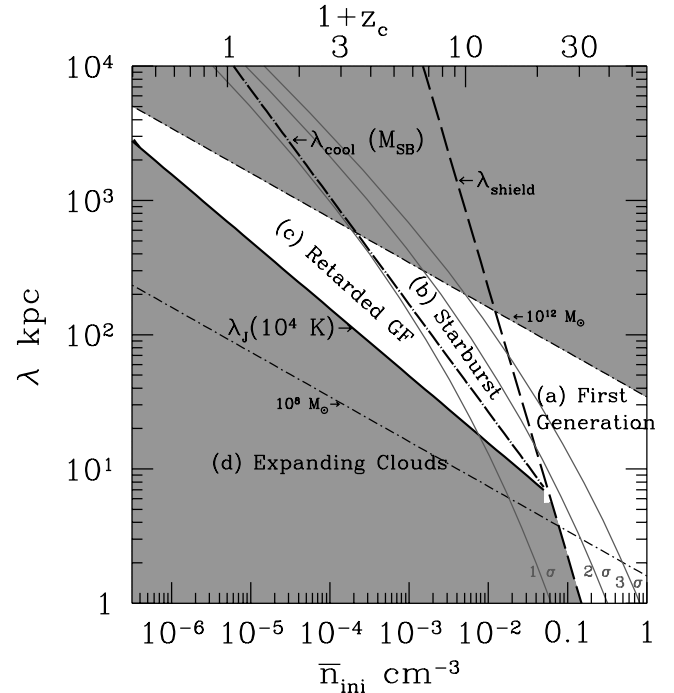

FIG. 7.—Initial parameter space is divided according to the evolution of clouds. Here, $\alpha = 1$ is assumed. Solid line, long-dashed line, dot-dashed line, and short-dashed line are the same as those in Fig. 5. The upper abscissa is the estimated redshifts of the final collapse, z_c. The dot-dashed line can be translated into $M_{SB} = 2.2 \times 10^{11}$ $M_\odot[(1 + z_c)/5]^{-4.2}$, if the initial stage is assumed to be at the maximum expansion. Thin dot-dashed lines denote the constant mass corresponding to $M = 10^8$ and 10^{12} $M_\odot$. Assuming a standard CDM cosmology, 1 σ, 2 σ, and 3 σ density fluctuations are also shown. The evolution of pregalactic clouds under UV background radiation branches off into four categories: (a) first generation (promptly self-shielded clouds), (b) starburst (initial starburst pancakes), (c) retarded GF (retarded star formation in primordial galaxies), and (d) expanding clouds (unbound UV-heated clouds).

we can expect the first generation of objects in the mass range of $10^6 M_\odot$ at $z_c = 15$ down toward $10^3 M_\odot$ at $z_c \gg 200$ (Tegmark et al. 1997).

5.2. Initial Starbursts in Pancakes

Region (b) in Figure 7 results in cold pancakes owing to H_2 cooling, in which initial starbursts may take place. The instability of a shock-compressed layer has been discussed by several authors (Elmegreen & Elmegreen 1978; Vishniac 1983; Lubow & Pringle 1993; Whitworth et al. 1994; Yamada & Nishi 1998). According to Elmegreen & Elmegreen (1978), the fastest growing modes have the size of the sheet thickness and the fragmentation timescale is $t_{frag} = [-4\pi\rho(0)w^2]^{-1/2}$, where $w^2 \sim -0.14$ in the high external pressure limit. We estimate the line mass l_0 at fragmentation by a condition $t_{frag} = t_{dyn}$, where $t_{dyn} = \rho(0)/\dot\rho(0)$. Under an assumption that cold ($T \lesssim 10^3$ K) sheets fragment into filaments, the resultant line mass is tabulated in Table 2 with other properties, where f is the ratio of l_0 to the critical line density $l_c \equiv 2kT_0/m_p G$, and x_s and x_c denote the mass fraction of the shocked matter and cooled matter, respectively. It is noted that f is smaller than unity for the fastest growing modes. Hence, for the fragmentation, it is necessary for other growing modes to accumulate further mass so that the filaments would be supercritical. The supercritical filaments would eventually bear massive stars (Nakamura & Umemura 1999).

We can estimate the minimum mass of the starburst pancakes by $M_{SB} \equiv \bar\rho_{ini} \lambda_{cool}^3$. Again, if the initial stage is at the maximum expansion, then

$$M_{SB} = 2.2 \times 10^{11} M_\odot \left(\frac{1 + z_c}{5}\right)^{-4.2} \left(\frac{\Omega_B h^2}{0.02}\right)^{-1.4}. \quad (22)$$

The collapse epochs of the clouds in region (b) range from $z_c \simeq 3$ to $z_c \simeq 10$. The clouds may undergo further shrinking after the sheetlike collapse because the rotation barrier is smaller by Λ_{spin}^2 than the maximum expansion size, where Λ_{spin} is the dimensionless spin parameter which is peaked around 0.05 (Heavens & Peacock 1988). Consequently, the violent relaxation would take place in a collisionless fashion. Hence, the starburst pancakes highly possibly lead to the dissipationless galaxy formation. It is worthy noting that M_{SB} lies between 1 σ and 2 σ fluctuations in a standard CDM scenario. Thus, they could form a relatively clustered population of galaxies.

5.3. Retarded Galaxy Formation

The clouds with a smaller mass than M_{SB} cannot cool below 10^4 K at the first pancake collapse, but they might pass λ_{shield} in the course of shrinking down to the rotation barrier, so that the clouds are self-shielded against external UV radiation to cool down by H_2 molecules. Assuming $\Lambda_{spin} = 0.05$, the marginal size, λ_{rot}, above which the clouds can pass λ_{shield} is much smaller than size of the Jeans-

unstable clouds for $z_c \geq 0$. Thus, no cloud can be stopped by the rotation barrier before the cloud is self-shielded. In the clouds in region (c), the star formation is likely to be retarded until the pancake disk shrinks considerably. Therefore, region (c) tends to result in the so-called dissipational galaxy formation (e.g., Larson 1976; Carlberg 1985; Katz & Gunn 1991). The collapse epochs are relatively later ($0 \lesssim z_c \lesssim 4$), compared to region (b), and region (c) is corresponding to CDM fluctuations lower than 1 σ. Thus, it is likely that region (c) leads to a less clustered population of galaxies. Futhermore, for low redshifts ($z \lesssim 1$), the intensity of the UV background is no longer at a level of $I_{21} = 0.1$ but could be smaller by 2 orders of magnitude (Maloney 1993; Henry & Murthy 1993; Dove & Shull 1994). Since $\lambda_{shield} \propto I_{21}$ for $\alpha = 1$ as seen in equation (21), the clouds with $z \lesssim 1$ in region (c) might cool quickly in the course of shrinking down to the rotation barrier.

5.4. Expanding Clouds

In region (d), the clouds are no longer gravitationally bound because of the enhancement of thermal pressure due to UV heating. They are relatively low-mass systems. They could be Lyα absorption systems that are seen in QSO spectra (Umemura & Ikeuchi 1984, 1983; Bond, Szalay, & Silk 1988).

6. CONCLUSIONS

We have numerically explored the thermal and dynamical evolution of pregalactic clouds under UV background radiation. The plane-parallel collapse of primordial gas clouds has been pursued, including chemical reactions with respect to hydrogen molecules as well as atomic hydrogen. Also, the radiation transfer for the ionizing photons has been properly treated. As a result, it is found that the cloud evolution under UV background branches off into four categories in the initial parameter space of density and size. They are (a) promptly self-shielded clouds, which evolve into dense objects with $\lesssim 10^6 M_\odot$ at collapse redshifts (z_c) greater than 10; (b) starburst pancake clouds with the mass higher than $M_{SB} = 2.2 \times 10^{11} M_\odot[(1 + z_c)/5]^{-4.2}$, which lead to the dissipationless galaxy formation at $3 \lesssim z_c \lesssim 10$; (c) retarded star-forming galaxies with the mass lower than M_{SB}, which undergo star formation in the course of shrinking down to the rotation barrier at $0 \lesssim z_c \lesssim 4$, consequently leading to the dissipational galaxy formation; and (d) less massive expanding clouds, which could be detected as Lyα absorbers in QSO spectra. If we assume a standard CDM cosmology, density fluctuations of 1 σ–2 σ coincides with M_{SB}. That is, fluctuations higher than 2 σ result in the dissipationless formation of massive galaxies at $3 \lesssim z_c \lesssim 10$ and eventually constitute a clustered population. From a further realistic point of view, there must be local subgalactic clumps growing in a pregalactic cloud in a bottom-up scenario as in a CDM cosmology. They are likely to be self-

TABLE 2
INITIAL PHYSICAL PARAMETERS AND THE PROPERTIES OF CYLINDRICAL FRAGMENTS

λ (kpc)	$\bar{n}_{ini}$ (cm^{-3})	l_0 ($M_\odot$ pc^{-1})	f	x_s (shocked)	x_c (cooled)
100......	1×10^{-3}	8.7×10^3	2.4×10^{-1}	0.54	Not cooled
100......	2×10^{-3}	6.3×10^2	1.7×10^{-1}	0.78	0.47
100......	1×10^{-2}	1.5×10^1	2.2×10^{-2}	0.36	0.31

APPENDIX

FREQUENCY INTEGRATION FOR PHOTOIONIZATION AND UV HEATING RATE

In this Appendix, a method to integrate the frequency dependence in radiation transfer equation is presented (see also Tajiri & Umemura 1998). This method is applied to plane-parallel calculations in this paper. However, it is also potent for the three-dimensional calculations on cosmic ionization problem (Nakamoto, Umemura, & Susa 2000). The frequency-dependent radiation transfer equation is given by a general form as

$$\boldsymbol{n} \cdot \nabla I_\nu = -\kappa_\nu I_\nu + \eta_\nu ,$$

(A1)

where $\boldsymbol{n}$ is the unit directional vector and κ_ν and η_ν denote the opacity and the emissivity, respectively. For the gas composed of pure hydrogen, the emissivity is almost null for $\nu \gtrsim \nu_L + \Delta\nu_T$, where $\Delta\nu_T$ denotes the width of the Lyman limit emission resulting from radiative recombination:

$$\Delta\nu_T \equiv kT/h_P ,$$

(A2)

where T, k, and h_P denote the gas temperature and Planck constant, respectively. Typically, $\Delta\nu_T/\nu_L \approx 0.1$ for $T = 10^4$ K. As far as higher energy photons of $\nu \gtrsim \nu_L + \Delta\nu_T$ are concerned, the solution of equation (A1) is simply

$$I_\nu = I_\nu^{in} \exp\left[-\tau_\nu(\omega)\right] ,$$

(A3)

where I_ν^{in} denotes the incident intensity at the boundary. The optical depth $\tau_\nu(\omega)$ in the solid angle ω is rewritten in terms of the optical depth at Lyman limit, $\tau_{\nu_L}(\omega)$,

$$\tau_\nu(\omega) = \tau_{\nu_L}(\omega)(\nu_L/\nu)^3 ,$$

(A4)

because the photoionization cross-section is $\sigma_\nu \simeq \sigma_{\nu_L}(\nu_L/\nu)^3$. Using equations (A3) and (A4), we obtain the photoionization rate coefficient for this energy range of photons, k_{HI}^{abs}, in terms of an integration as

$$k_{HI}^{abs} = \int_{\nu_L + \Delta\nu_T}^{\infty} \int \frac{I_\nu}{h\nu} \sigma_\nu \, d\omega \, d\nu ,$$

$$\simeq \frac{I_{\nu_L}^{in} \sigma_{\nu_L}}{h} \int \frac{1}{3\tau_{\nu_L}(\omega)^{1+\alpha/3}} \gamma\left[1 + \frac{\alpha}{3}, \tau_{\nu_L}(\omega)\right] d\omega ,$$

(A5)

$$\propto \tau_{\nu_L,\nu}^{-1-\alpha/3} \qquad (\tau_{\nu_L,\nu} \ll 1) ,$$

(A6)

where we have assumed $I_\nu^{in} = I_{\nu_L}^{in}(\nu/\nu_L)^{-\alpha}$ and $\gamma(a, b)$ denotes the incomplete gamma function. $\tau_{\nu_L,\nu}$ denotes the optical depth measured in the vertical directions of a slab, which has already been introduced in § 4. It is noted that the integration in frequency space has been carried out just analytically with the incomplete gamma function. In other words, we do not have to solve the radiation transfer equation for $\nu \gtrsim \nu_L + \Delta\nu_T$.

On the other hand, photons with $\nu_L \leq \nu \leq \nu_L + \Delta\nu$ are scattered to produce diffuse radiation. For hydrogen, the scattering albedo is given by $[\alpha_A(T) - \alpha_B(T)]/\alpha_A(T)$, where $\alpha_A(T)$ is the total recombination coefficient to all bound levels and $\alpha_B(T)$ is the recombination coefficient to all *excited* levels. Hence, we have to integrate the radiation transfer equation including the emissivity by scatterings. In this frequency range, the frequency dependence of the opacity and the emissivity are thought to be smal because $\Delta\nu_T$ is 10 times smaller than ν_L for $T = 10^4$ K. So, we approximate the opacity and emissivity to be constant in this frequency range. After the transfer equation is solved, we calculate the angle averaged intensity J_{ν_L} in terms of the numerical solution I_{ν_L}. Using J_{ν_L}, we obtain the photoionization rate coefficient for this frequency range, k_{HI}^{sca};

$$k_{HI}^{sca} \simeq 4\pi \frac{J_{\nu_L} \sigma_{\nu_L}}{h\nu_L} \Delta\nu_T .$$

(A7)

Finally, by adding equation (A6) to equation (A7), we obtain the total ionization rate k_{HI};

$$k_{HI} = k_{HI}^{abs} + k_{HI}^{sca} .$$

(A8)

The UV heating rate $\Gamma_{\rm H\,I}$ is also obtained in a similar way. The result is,

$$\Gamma_{\rm H\,I} = \Gamma_{\rm H\,I}^{\rm abs} + \Gamma_{\rm H\,I}^{\rm sca} , \tag{A9}$$

$$\Gamma_{\rm H\,I}^{\rm abs} = \int_{v_L + \Delta v_T}^{\infty} \int \frac{I_\nu}{h\nu}\, \sigma_\nu (h\nu - h\nu_L) d\omega\, d\nu ,$$

$$\simeq \frac{I_{\nu_L}^{\rm in} \sigma_{\nu_L}}{h} \int \frac{1}{3\tau_{\nu_L}(\omega)^{1+(\alpha-1)/3}}\, \gamma\left[1 + \frac{(\alpha-1)}{3}, \tau_{\nu_L}(\omega)\right] h\nu_L\, d\omega - h\nu_L\, k_{\rm H\,I}^{\rm abs} , \tag{A10}$$

$$\Gamma_{\rm H\,I}^{\rm sca} \simeq 4\pi J_{\nu_L} \sigma_{\nu_L} \Delta\nu_T . \tag{A11}$$

In particular, for an infinite sheet, we have an asymptotic expression for the absorption part $(\Gamma_{\rm H\,I}^{\rm abs})$ in an optically thick limit as

$$\Gamma_{\rm H\,I}^{\rm abs} \simeq \frac{2\pi I_{\nu_L}^{\rm in} \sigma_{\nu_L} \nu_L}{3}\, \frac{\Gamma[1+(\alpha-1)/3]}{2+(\alpha-1)/3}\, \tau_{\nu_L,v}^{-1-(\alpha-1)/3} , \tag{A12}$$

where $\Gamma(a)$ represents the gamma function. It should be noted that the UV heating rate is not proportional to $\exp(-\tau_{\nu_L,v})$ but, rather, is proportional to $\tau_{\nu_L,v}^{-1-(\alpha-1)/3}$ for large $\tau_{\nu_L,v}$. If we choose $\alpha = 1$ as in the present paper, the UV heating rate is proportional to $\tau_{\nu_L,v}^{-1}$. This shallow dependence upon the optical depth comes from a steep dependence of ionization cross section upon frequencies.

REFERENCES

Abel, T., & Haehnelt, M. G. 1999, ApJ, 520, L13
Anninos, P. A., & Norman, M. L. 1996, ApJ, 460, 556
Babul, A., & Rees, M. J. 1992, MNRAS, 255, 346
Bajtlik, S. Duncan, R. C., & Ostriker, J. P. 1988, ApJ, 327, 570
Beiniek, R. J. 1980, J. Phys. B, 13, 4405
Bertoldi, F., & Draine, B. T. 1996, ApJ, 458, 222
Blumenthal, G. R., Faber, S. M., Primack, J. R., & Rees, M. J. 1984, Nature, 311, 517
Böhringer, H., & Hensler, G. 1989, A&A, 215, 147
Bond, J. R., Centrella, J., Szalay, A. S.,& Wilson, J. R. 1984, MNRAS, 210, 515
Bond, J. R., Szalay, A. S., & Silk, J. 1988, ApJ, 324, 627
Carlberg, R. G. 1981, MNRAS, 197, 1021
———. 1985, ApJ, 298, 486
Cen, R., Miralda-Escudé, J., Ostriker, J. P., & Rauch, M. 1994, ApJ, 437, L9
Chiba, M., & Nath, B. 1994, ApJ, 436, 618
Cole, S., Aragon-Salamanca, A., Frenk, C. S., Navarro, J. F., & Zepf, S. E. 1994, MNRAS, 271, 781
Colella, P., & Woodward, P. R. 1984, J. Comp. Phys., 54, 174
Corbelli, E., Galli, D., & Palla, F. 1997, ApJ, 487, 53L
Cowie, L. L., & Songaila, A. 1998, Nature, 394, 44
Cowie, L. L., Songaila, A., Kim, T., & Hu, E. M. 1997, AJ, 109, 1522
de Jong, T. 1972, A&A, 20, 263
Dekel, A., & Rees, M. J. 1987, Nature, 326, 455
Diaz-Miller, R. I., Franco, J., & Shore, S. N. 1998, ApJ, 501, 192
Dove, J. B., & Shull, M. 1994, ApJ, 423, 196
Draine, B. T., & Bertoldi, F. 1996, ApJ, 468, 269
Duley, W. W., & Williams, D. A. 1984, Interstellar Chemistry (London: Academic)
Efstathiou, G. 1992, MNRAS, 256, 43
Elmegreen, B. G., & Elmegreen, D. M. 1978, ApJ, 220, 1051
Giallongo, E., Cristiani, S., D'Odorico, S., Fontana, A., & Savaglio, S. 1996, ApJ, 466, 46
Gunn, J. E., & Peterson, B. A. 1965, ApJ, 142, 1633
Haiman, Z., Rees, M. J., & Loeb, A. 1996, ApJ, 467, 522
———. 1997, ApJ, 476, 458
Heavens, A., & Peacock, J. 1988, MNRAS, 232, 339
Henry, R. C., & Murthy, J. 1993, ApJ, 418, L17
Hernquist, L., Katz, N., Weinberg, D. H., & Miralda-Escude, J. 1995, ApJ, 457, L51
Hollenbach,D. J., & McKee, C. 1979, ApJS, 41, 55
Hollenbach,D. J., & Tielens, A. G. G. M. 1999, Rev. Mod. Phys., 71, 173
Hutchins, J. B. 1976, ApJ, 205, 103
Izotov, Yu.I., & Kolensnik, I.G. 1984, Soviet Astron., 28, 15
Kang, H., & Shapiro, P. 1992, ApJ, 386, 432
Karpas, Z.,Anicich, V., & Huntress, W.T., Jr. 1979, J. Chem. Phys., 70, 2877
Katz, N., & Gunn, J. E. 1991, ApJ, 377, 365
Kauffmann, G., White, S. D. M., & Guiderdoni, B. 1993, MNRAS, 264, 201
Kepner, J., Babul, A., & Spergel, N. 1997, ApJ, 487, 61
Larson, R. B. 1976, MNRAS, 176, 31

Lotz, W. 1968, Zs. Phys., 216, 241
Lubow, S. H., & Pringle, J. E. 1993, MNRAS, 263, 701
Maloney, P. 1993, ApJ, 414, 41
Matsuda, T., Sato, H., & Takeda, H. 1969, Prog. Theor. Phys., 42, 219
Miralda-Escude, J., & Rees, M. J. 1994, MNRAS, 266, 343
Mitchell, G. F., & Deveau, T. J. 1983, ApJ, 266, 646
Nakamoto, T., Umemura, M., & Susa, H. 2000, MNRAS, submitted
Nakamura, F., & Umemura, M. 1999, ApJ, 515, 239
Navarro, J., & Steinmetz, M. 1997, ApJ, 478, 13
Osterbrock, D. E. 1989, Astrophysics of Gaseous Nebula & Active Galactic Nuclei (Mill Valley: University Science Books)
Palla, F., Salpeter, E. E., & Stahler, S. W. 1983, ApJ, 271, 632
Poularert, G., Brouillard, F., Claeys, W., McGowan, J. W., & Van Wassenhove, G. 1978, J. Phys. B, 11, L671
Prasad, S. S., & Huntress, W. T., Jr. 1980, ApJS, 43, 1
Quinn, T., Katz, N., & Efstathiou, G. 1996, MNRAS, 278, L49
Ramaker, D. E., & Peek, J. M. 1976, Phys. Rev. A, 13, 58
Rees, M. J., & Ostriker, J. P. 1977, MNRAS, 179, 541
Schneider, D. P., Schmidt, M., & Gunn, J. E. 1989, AJ, 98, 1951
———. 1991, AJ, 102, 837
Shapiro, P. R., & Kang, H., 1987, ApJ, 318, 32
Shapiro, P. R., & Struck-Marcell, C. 1985, ApJS, 57, 205
Shapiro, P. R., Struck-Marcell, C., & Melott, A. L. 1983, ApJ, 275, 413
Songaila, A. 1997, ApJ, 490, L1
Songaila, A., & Cowie, L. L. 1996, AJ, 112, 335
Spitzer, L., Jr. 1956, The Physics of Fully Ionized Gases (New York: Interscience)
———. 1978, Physical Processes in the Interstellar Medium (New York: Wiley)
Stone, J. M., Mihalas, D., & Norman, M. L. 1992, ApJS, 80, 819
Susa, H., Uehara, H., & Nishi, R. 1996, Prog. Theor. Phys., 96, 107
Susa, H., Uehara, H., Nishi, R., & Yamada, M. 1998, Prog. Theor. Phys., 100, 63
Tajiri, Y., & Umemura, M. 1998, ApJ, 502, 59
Tegmark, M., Silk, J., Rees, M. J., Blanchard, A., Abel, T., & Palla, F. 1997, ApJ, 474, 1
Thoul, A. A., & Weinberg, D. H. 1996, ApJ, 465, 608
Uehara, H., Susa, H., Nishi, R., & Yamada, M. 1996, ApJ, 473, L95
Umemura, M. 1993, ApJ, 406, 361
Umemura, M., & Ikeuchi, S. 1984, Prog. Theor. Phys., 72, 47
Vishniac, E. T. 1983, ApJ, 274, 152
White, S. D. M., & Frenk, C. S. 1991, ApJ, 379, 52
Whitworth, A. P., Bhattal, A. S., Chapman, S. J., Disney, M. J., & Turner, J. A. 1994, A&A, 290, 421
Yamada, M., & Nishi, R. 1998, ApJ, 505, 148
Yoneyama, T. 1972, PASJ, 24, 87
Yuan, W., Centrella, J. M., & Norman, L. M. 1991, ApJ, 376, L29
Zeldovich, Ya. B. 1970, A&A, 5, 84
Zhang, Y., Anninos, P., & Norman, M. 1995, ApJ, 453, L57